communications chemistry

ARTICLE

https://doi.org/10.1038/s42004-023-00865-x OPEN

The highest oxidation state observed in graphene-supported sub-nanometer iron oxide clusters

Deborah Perco [1], Federico Loi [1], Luca Bignardi [1], Luca Sbuelz[1], Paolo Lacovig [2], Ezequiel Tosi[2], Silvano Lizzit[2], Aras Kartouzian [3], Ueli Heiz[3] & Alessandro Baraldi [1,2]✉

Size-selected iron oxide nanoclusters are outstanding candidates for technological-oriented applications due to their high efficiency-to-cost ratio. However, despite many theoretical studies, experimental works on their oxidation mechanism are still limited to gas-phase clusters. Herein we investigate the oxidation of graphene-supported size-selected Fe_n clusters by means of high-resolution X-ray Photoelectron Spectroscopy. We show a dependency of the core electron Fe $2p_{3/2}$ binding energy of metallic and oxidized clusters on the cluster size. Binding energies are also linked to chemical reactivity through the asymmetry parameter which is related to electron density of states at the Fermi energy. Upon oxidation, iron atoms in clusters reach the oxidation state Fe(II) and the absence of other oxidation states indicates a Fe-to-O ratio close to 1:1, in agreement with previous theoretical calculations and gas-phase experiments. Such knowledge can provide a basis for a better understanding of the behavior of iron oxide nanoclusters as supported catalysts.

[1] Department of Physics, University of Trieste, Via Valerio 2, 34127 Trieste, Italy. [2] Elettra - Sincrotrone Trieste, AREA Science Park, 34149 Trieste, Italy. [3] Department of Chemistry, Technical University of Munich, Lichtenbergstrasse 4, 85748 Garching, Germany. ✉email: alessandro.baraldi@elettra.eu

The quest for newly designed and efficient catalysts is a central issue that has attracted the interests of many researchers since it constitutes the essential stage to enhance the sustainability of many chemical processes of industrial relevance. In this respect, the possibility to prepare metallic-based nanostructures has provided a potentially groundbreaking way to improve the efficiency of traditionally designed catalysts and has been gaining interest in the scientific community in the last years[1,2]. Among the various nanostructured materials proposed and investigated, size-selected atomic clusters constitute a special class of objects whose properties depend strongly also on the number of atoms composing them and which have shown astounding catalytic performances[3–5]. The use of iron in these systems is of recent application. While Fe metal-based catalysts have been proven since long time to be crucial in industrially relevant reactions such as the Haber-Bosch process[6–9], Fe atomic clusters stood out as potential candidate to substitute the highly expensive noble metal-based catalysts in the oxygen reduction reaction[10–13], in the ammonia synthesis[14] and for the alkene epoxidation[15]. The range of interest for Fe-based nanostructures further increases if we include Fe oxides[16,17], which find several technological applications as magnetic storage media[18], in biomedicine[19] and as catalysts in several chemical reactions such as CO oxidation[20–24], water splitting[25] and in the Water Gas Shift[26]. Like their bulk counterparts, the properties of a specific Fe oxide cluster depend on its stoichiometry and oxidation state. For example, Fe_2O_3 cluster can oxidize CO to form CO_2 and reduce NO to form N_2 by undergoing compositional changes between Fe_2O_2 and Fe_2O_3 states[27]. A deep understanding of the intrinsic factors that determine the properties of oxide clusters is still lacking and it represents a hot topic in the scientific community as demonstrated by several theoretical results published in the last few years on Fe_nO_m clusters[28–32]. While theory has highlighted the interest for these materials, experiments on the oxidation of Fe clusters are mainly limited to the gas phase[33–36], which represents a fundamental approach for the understanding of these systems and for a comparison with theoretical works, but it is still far from the complexity of supported catalysts.

In the present work, we studied the oxidation of size-selected Fe_n clusters with $n = 11$, 12, 13, 15 and 20 supported on graphene epitaxially grown on Ru(0001) by means of high-resolution X-Ray Photoelectron Spectroscopy with synchrotron radiation. Clusters were then oxidized with a photodissociation approach (Fig. 1). We have chosen to study Fe_{13} and Fe_{15} since they are magic clusters[37–39] and have been already predicted to show enhanced stability and remarkable properties. At the same time, we intended to investigate some non-magic clusters whose size is larger and smaller than the two aforementioned magic ones, in order to showcase any remarkable differences. For example, recent density functional theory (DFT) calculations predicted that the 12 cluster shows an uncommon stability in the stoichiometry $Fe_{12}O_{12}$[40]. In this work we show that upon oxidation all the atoms in the supported Fe_n clusters can reach a maximum oxidation state equal to Fe(II), in agreement with theoretical works which predict a high stability for $(FeO)_n$ clusters[41]. The differences between the stability of Fe(II) oxidation state in the nanocluster and in solid surfaces highlight the different behavior of iron oxides at sub nanoscale.

Results and discussion

Spectroscopic characterization of metallic Fe_n clusters. Fe_n^+ nanoclusters with $n = 11$, 12, 13, 15 and 20 were deposited on graphene/Ru(0001), where they are electrically neutralized. Graphene/Ru(0001) is a very stable and highly corrugated 2D material which was already adopted for the growth and deposition of atomic clusters[42,43]. The morphology of this template reduces the cluster mobility as they tend to remain confined in the valley regions of the moiré lattice[44]. In fact, despite the calculated large adsorption energy of Fe adatoms on free standing graphene, $E_a = 0.85$ eV, the diffusion barrier is only 0.40 eV[45], thus indicating that they are mobile at room temperature. To reduce the cluster mobility and to prevent sintering and nucleation, the temperature of the system was always kept at T = 20 K during the deposition and photoemission measurements. It is worth noting that the diffusion rate Γ on a surface follows the formula $\Gamma = \nu \exp^{-\Delta E/k_B T}$, where ν is the vibrational frequency of the adatom, ΔE is the diffusion barrier, k_B is the Boltzmann constant and T the surface temperature. Using a prefactor ν equal to 10^{13}, the diffusion rate that is obtained at room temperature is equal to $1.7 \times 10^6\ s^{-1}$. On the other hand, at $T = 20$ K the rate becomes equal to $1.75 \times 10^{-88}\ s^{-1}$, meaning that the diffusion of iron adatoms on graphene at a very low temperature is highly suppressed and become negligible on the time scale of our deposition and data acquisition.

The Fe $2p_{3/2}$ core level spectra of the supported pristine clusters are reported in Fig. 2a, together with the best fit and the spectral components. The very low cluster coverage on graphene (<0.1% ML), the low photoionization cross section and the large intrinsic broadening of 2p core levels (especially when compared to the 3d and 4f core levels, which are typically studied for heavier metals), make the data analysis particularly challenging. Such analysis, performed using Doniach-Šunjić functions[46] convoluted with a Gaussian distribution, requires a rigorous procedure to obtain reliable information not only on the Fe 2p core level binding energies (BE) and of the number of non-equivalent components, but also of the core level photoemission line shape parameters, namely Gaussian (G) and Lorentzian (L) widths, and asymmetry (α). In this convolution, the Lorentzian lineshape L takes into account the core-hole lifetime through the uncertainty principles. The Gaussian width originates from several factors including the instrumental resolution, the phonon/vibrational broadening together with the inhomogeneous broadening due to the presence of a distribution of non-equivalent atomic configurations. The Anderson singularity index α describes the asymmetry of the lineshape due to the probability of electron-hole pairs excitation. The decision of using the Doniach-Šunjić function convoluted with a Gaussian distribution rather than the Voigt function, often preferred for quantitative analysis[47], is justified by the fact that we are not interested in a composition analysis of the oxidized iron clusters, but in obtaining information about the asymmetry when it is present, as in clusters spectra before the oxidation process. Doniach-Šunjić functions convoluted with a Gaussian distribution have been extensively used in literature for fitting both metallic and oxidized surfaces[48,49]. Moreover, recently their use has been extended to properly fit the spectra of oxide nanoparticles and gas-phase nanoclusters[50,51]. Thus, we decided to fit XPS spectra of oxidized iron clusters using a Doniach-Šunjić function convoluted with a Gaussian distribution. This choice is motivated also by the results of Bano et al.[52] which show that, on graphene, the HOMO-LUMO gap of iron oxide clusters is close to zero, allowing the use of this fitting function. This is due to a charge-transfer between graphene and clusters that involves also a semi-metal to metal transition of the graphene itself. Generally, it is important to point out that the Doniach-Šunjić function convoluted with a Gaussian distribution becomes a Voigt function when the value of α approaches to zero, as in our case. Since iron is a ferromagnetic material, the $2p_{3/2}$ core level measured on surfaces of single crystals is described using four components that mainly originates from exchange interactions[53–55]. However, since the signal-to-noise ratio in

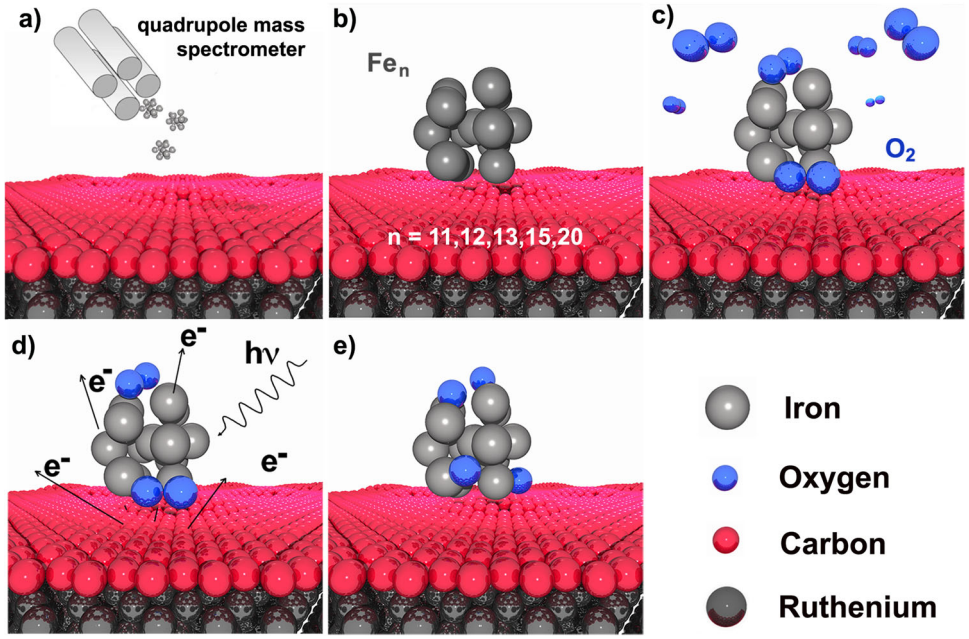

Fig. 1 Outline of the oxidation process. a Fe clusters deposition on Gr/Ru(0001) **b** Adsorbed Fe cluster on the Gr/Ru(0001) interface. **c** O_2 exposure at 20 K and physisorption on the Fe cluster at 20 K. **d** Emission of low-energy secondary electrons induced by soft x-ray irradiation. **e** Formation of atomic oxygen via dissociation of molecular oxygen and cluster oxidation.

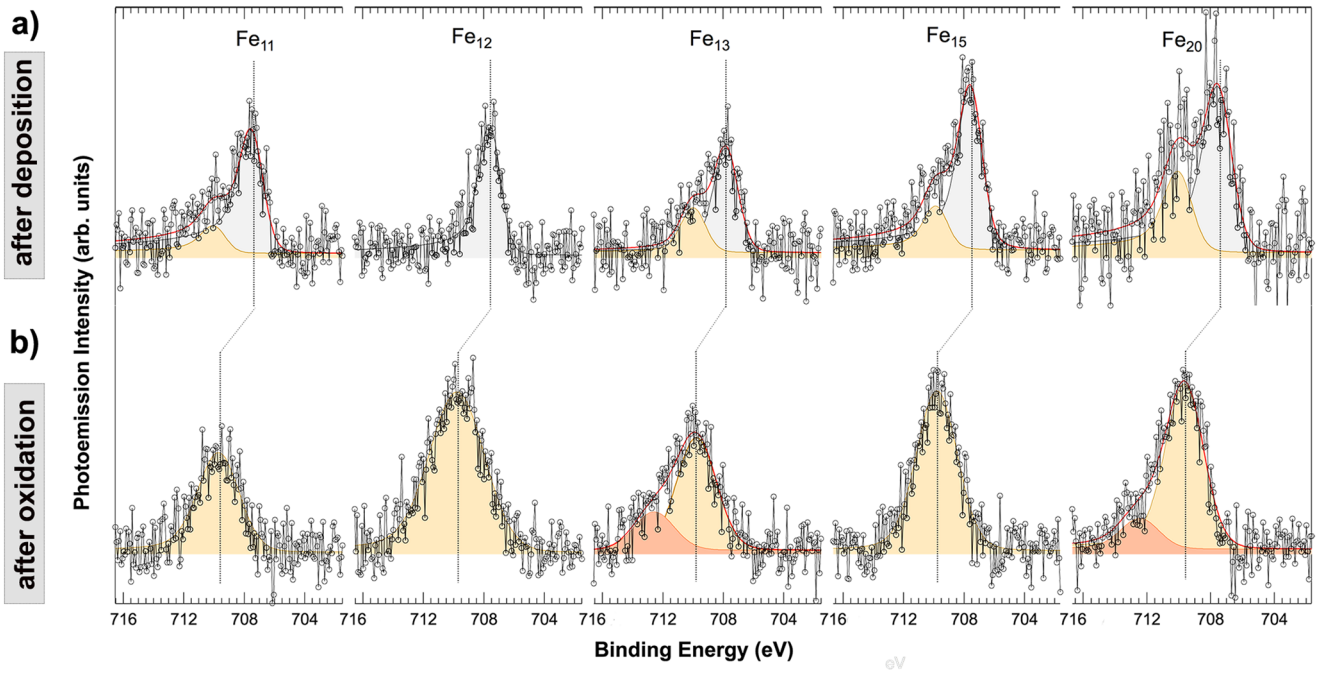

Fig. 2 X-ray photoelectron spectra of as deposited and oxidized clusters. a Fe $2p_{3/2}$ core level spectra for as deposited and **b** oxidized Fe_{11}, Fe_{12}, Fe_{13}, Fe_{15} and Fe_{20} nanoclusters supported on graphene/Ru(0001). Black markers and lines represent experimental data, the red line represents the best fit. Each peak stemming from the spectral analysis is shown in a different color. For the labeling of each peak please refer to the text.

our spectra is low and since in literature the splitting between the components spans between 0.35 eV and 0.5 eV, we decided to fit our spectra using one single component. This choice is motivated also by the presence of a plethora of non-equivalent atoms in each cluster that would require using a number of components equal to 4n for the spectra of Fe_n clusters. The small error bar on the binding energy values of the different spectral components stemming from the fit, and reported in Table 1, is due to the complex fit procedure applied for interpreting the data and that is characterized by consecutive steps of analysis to extract the best fit parameters, as discussed in the Supplementary Note 1.

The spectral analysis in Fig. 2a indicates the presence of two different components for each of the investigated clusters besides Fe_{12}. The position of the low BE component, which exhibits most of the spectral weight (Fig. 2a, gray curves), is affected non-monotonically by the cluster size, ranging from 707.38 eV for Fe_{11} and Fe_{20} up to 707.77 eV for Fe_{13} (Tab. 1). This component can be associated to Fe atoms in a metallic state. The shift towards

Table 1 BE in metallic and oxidized Fe-base materials.

Fe clusters			
Metallic		**Oxide**	
	BE (eV)		BE (eV)
Fe_{11}	707.38 ± 0.10 ; 709.87 ± 0.10	Fe_{11}	709.62 ± 0.10
Fe_{12}	707.50 ± 0.10	Fe_{12}	709.68 ± 0.10
Fe_{13}	707.77 ± 0.10 ; 709.92 ± 0.10	Fe_{13}	709.79 ± 0.10 ; 712.59 ± 0.10
Fe_{15}	707.47 ± 0.10 ; 709.75 ± 0.10	Fe_{15}	709.77 ± 0.10
Fe_{20}	707.38 ± 0.10 ; 709.87 ± 0.10	Fe_{20}	709.58 ± 0.10 ; 712.39 ± 0.10
Fe Bulk and Surfaces			
Metallic		**Oxide**	
	BE Fe^0 (eV)		BE Fe^{2+} (eV)
Fe bulk	706.7[56]	FeO bulk	709.5[57]
Fe(100)/Cu(100)	706.5[57]	Oxidized Fe(100)/Cu(100)	709.2[57]
Fe(110)/Cu(100)	706.3[57]	Oxidized Fe(110)/Cu(100)	709.3[57]
Fe Polycrystal	706.28 ± 0.10	Oxidized Fe polycrystal	709.83 ± 0.10

Fe $2p_{3/2}$ core level BE for metallic and oxidized Fe clusters and polycrystal, as obtained from data analysis, and Fe bulk and surfaces, as reported in literature. Error analysis is described in Supplementary Note 1.

higher BE with respect to Fe bulk (BE = 706.7 eV)[56], single crystal surfaces (BE = 706.3 for Fe(110)/Cu(100) and 706.5 eV for Fe(100)/Cu(100)[57]) and to Fe polycrystal (BE = 706.28 eV, Supplementary Note 2) is in agreement with previous measurements on supported Pd and Au clusters on oxides[58,59]. For these systems, 3d and 4f core level shifts (CLS) were generally attributed to final state effects due to a size-dependent charging energy which scales with $n^{-1/3}$ [60]. However, the same model may not apply to our system, as the graphene/metal interface allows for charge transfer to the Fe clusters. A possible explanation to this experimental outcome may be linked to initial-state effects stemming from a lattice parameter contraction, which could significantly affect the CLS of the metallic Fe clusters, as proposed by Richter et al.[61]. Such guess appears to be reasonable since it is known that lattice strain causes a positive CLS: a strain of 6% in Cu, Ag and Au clusters composed of 13 atoms leads to a CLS of +0.79, +0.52 and +0.50 eV, respectively[62]. According to DFT calculations, the Fe − Fe distance in small Fe clusters in gas phase varies between 2.38 Å and 2.62 Å[37] with a contraction in the range of 8 − 18% with respect to the value of iron bulk (2.86 Å[63]). The CLS that we report for iron nanoclusters range between +0.68 and +1.07 eV, thus in agreement with the general trend that enhanced contraction of the lattice parameter generates a larger CLS. An additional contribution to the shift could arise from the interaction of the cluster with graphene[64] since the Fe-graphene bond strenght is not negligible, contrary, for example, to the case of Ag atoms[45].

The agreement between the measured BE of the clusters and the expected CLS due to lattice strain suggests that the CLS in the clusters are dominated by initial state effects. Initial state effects are rich in chemical information as they depend also on the modifications of the d-band center, a well-known indicator of chemical reactivity[65]. For this reason, their dominant contribution to the overall CLS allows us to relate the reactivity of clusters with different sizes to their Fe $2p_{3/2}$ core level BE, with a low activity that can generally be associated to higher-than-expected BE, and vice versa[58].

In Fig. 3a (black markers) we report the CLS of the clusters Fe $2p_{3/2}$ core level with respect to the bulk value as a function of the cluster size. Fe_{13} shows the largest CLS (+1.07 eV), thus suggesting that this cluster is the most stable among the examined ones. Interestingly 13 is a magic number for Fe clusters associated to particularly stable configurations and, therefore, it is expected to show a low chemical reactivity[38,39]. The CLS trend we measured is in good agreement also with the trend of the asymmetry parameter α obtained from the spectral analysis. The α parameter in the Doniach-Šunjić function, is directly linked to the probability to excite single-electron excitations, namely electron-hole pairs, and it is hence related to the density of states near the Fermi level of the system[46]. It is interesting to note that a higher density of states near the Fermi level has been linked to an increased reactivity of the system increased[66]. The trend of α*vs.* the cluster size n is reported in Fig. 3a (blue markers) together with the CLS trend. The two curves match very well for all the cluster sizes, supporting our discussion on the relationship between clusters reactivity and CLS.

Cluster oxidation and assignment of oxidation state. Nanoclusters oxidation was obtained employing a photo-dissociation approach at $T = 20$ K. At this temperature, it is possible to achieve a high degree of oxidation inducing the O_2 dissociation by soft x-rays irradiation as schematically described in Fig. 1[43,67–69]. After being exposed to molecular oxygen (Fig. 1b), iron nanoclusters were irradiated with soft x-rays (Fig. 1c). We irradiated the sample for an overall exposure of 2×10^{16} photons $s^{-1}cm^{-2}$, with a X-ray photon energy of 805 eV for ca. 45 min. The photo-stimulation induces the production of secondary low-energy electrons thus resulting in O_2 dissociation and atomic oxygen formation (Fig. 1d). The process of photo-electrons interaction with weakly bound physisorbed molecular oxygen results in intramolecular vibrational excitations via inelastic scattering. The effect has been proven using both photons and electrons, also by means of tunneling process employing scanning tunneling microscopy[70–72]. The oxidation of Fe nanoclusters results in a $2p_{3/2}$ CLS towards higher BEs (see Fig. 2b), confirming the well established trend found for Fe surfaces[73–75]. This component appears at the same BE of the low intensity peak revealed in the as-deposited clusters spectra (orange peaks in Fig. 2a), due to a partial oxidation of Fe cluster during deposition.

The Fe $2p_{3/2}$ core level spectra of oxidized Fe_{11}, Fe_{12} and Fe_{15} nanoclusters can be fitted using a single component (Fig. 2b, yellow curve), while an additional component at higher BE (Fig. 2b, orange curve) was needed to obtain a low chi-square in the spectral analysis corresponding to the oxidized Fe_{13} and Fe_{20}

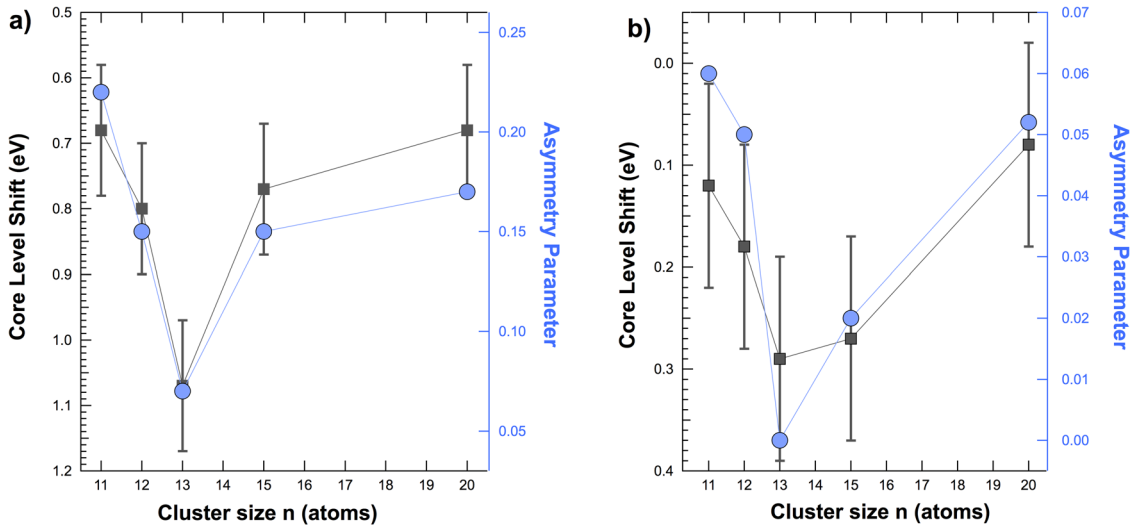

Fig. 3 Comparison CLS vs asymmetry parameter. a Core level α parameters and CLS of metallic and **b** oxidized iron clusters as a function of their size. Circle markers refer to asymmetry parameter while square markers refer to CLS. The error bars on the core level shifts are of the order ± 0.1 eV.

clusters spectra. As happens for the BE of the metallic clusters, the Fe $2p_{3/2}$ BE of oxidized clusters is clearly affected by their size. The main component (yellow curve) ranges from 709.58 eV for Fe_{11} to 709.79 eV for Fe_{13} (Tab. 1). If compared to the metallic configurations, these BEs are closer to the Fe $2p_{3/2}$ core level of the bulk, surfaces and polycrystal Fe oxides, which are reported in Tab. 1. This is interpreted as a consequence of the Fe-O bond lengths in the clusters (1.81 − 1.96 Å)[41] which become more similar to their bulk counterparts (1.98 Å for Fe_2O_3 and 2.09 Å for FeO[16]) than the Fe-Fe bond lenghts in the metallic case.

The asymmetry parameter α of the clusters decreases upon oxidation, going from the range 0.07–0.22 for metallic clusters down to 0.00 - 0.06. The trend of α still follows the CLS and it indicates that a higher chemical reactivity can be expected from oxidized clusters Fe_{11} and Fe_{20}, which show the lowest CLS and the highest asymmetry (Fig. 3b). The same trend suggests that the least reactive oxidized clusters are Fe_{13} and Fe_{15}, similarly to the metallic case. By comparison with previous XPS experiments, the main component in the oxidized spectra can be associate to Fe(II) ions (BE = 709.5 eV)[56,76]. Since our clusters are electrically neutral and all the Fe atoms possess the oxidation state 2 + , if we assume that O anions have the usual oxidation state 2 − , then we can conclude that the ratio between Fe and O atoms is close to 1:1. As a matter of fact, if we had a higher ratio, with more Fe than O atoms, we would expect to observe additional spectral components associated to Fe atoms with lower oxidation state or bonded with a lower number of O atoms. For example, the cage-like structure of the magic cluster $Fe_{13}O_8$ displays a Fe atom in its core in the metallic state[77]. Since from our spectra we can disregard the presence of atoms in a metallic state, we can exclude a similar Fe:O ratio. At the same time, if we had more O than Fe atoms in our clusters, we would expect to observe a component in the Fe $2p_{3/2}$ spectra compatible with Fe(III). The nominal BE value of the Fe(III) oxidation state is close to 711 eV[76]. The lack of compatible signal in the vicinity of this energy suggests that this oxidation state is most probably not present in the clusters. However, due to the different geometric and electronic properties of the clusters compared to bulk materials, the BE of the Fe(III) oxidation state could be shifted with respect to the nominal value[78,79]. Therefore, also considering the large FWHM of the spectra, it is not possible to unambiguously rule out the presence of Fe(III) species. However, these species would represent a minor fraction of the spectra, which are dominated by the Fe(II), supporting the conclusion that the ratio between Fe and O atoms is close to 1.

The formation of Fe(III) compounds has been ruled out because of the lack of compatible signal in the vicinity of BE = 711 eV[76], which is the expected position of Fe(III) compounds in bulk materials. Although there might be differences in the position of the components in bulk and clusters, we observed that such differences are not so large for 2+ oxidation state (with a shift ranging from 0.08 up to 0.29 eV with respect to the value observed for bulk). Likewise, we do not expect larger differences for the peaks associated to the 3+ oxidation state. In addition to that, whereas there would be any Fe(III) components, they would constitute a negligible fraction, since their spectral weight is very small with respect to the overall signal.The interpretation of the component at higher BE observed for Fe_{13} and Fe_{20} oxidized clusters (BE = 712.59 eV and 712.39 eV, respectively) requires a further explanation. Although it has been proposed that a component at such binding energy could stem from the presence of $FeCO_3$[56], the formation of such compound would locally disrupt the graphene lattice on which the clusters are laying. On the other hand, it seems reasonable to assume that this component could originate from Fe atoms at the bottom of the cluster and interacting with the graphene layer underneath. Upon larger oxygen exposures, the Fe $2p_{3/2}$ spectrum does not further change, indicating that this configuration is associated to the highest oxidation state and oxygen coverage that the clusters can reach upon oxidation with atomic oxygen.

Our result for supported Fe clusters is also in agreement with theoretical predictions on the stability of the stoichiometry Fe_nO_n for clusters of these sizes[41,80], and with experimental findings on the oxidation of Fe clusters in the gas phase[33]. In particular, DFT calculations showed that $Fe_{12}O_{12}$ possesses unexpected stability and an extremely large band gap of 2.00 eV[40]. However, the same cluster shows several isomers separated only by few meV[80]. For example, the cage-shaped minimum energy configuration is favored by just 0.07 eV with respect of two tower structures composed of 3 × 3 and 4 × 4 rings which are nearly degenerate, with an energy difference of just 0.01 eV. The presence of different isomers can be read in our experiment from the Gaussian width (G value) obtained in the data analysis which is much larger than the overall experimental resolution. The oxidized Fe_{12} cluster shows the largest G value (4.12 eV) among the other oxidized clusters (G = 2.63 − 3.04 eV), thus suggesting

that it could be the cluster with highest number of isomers, i.e., with a large distribution of non-equivalent local atomic configurations. We associate the increased G values of oxidized clusters with respect to the metallic ones ($G = 1.51 - 1.83$) to the larger number of non-equivalent local configurations that the oxygen adsorption leads to. As a matter of fact, given a certain number of metallic isomers which contribute to the Gaussian broadening for the spectra after deposition, each one can lead to several oxide structures for a specific oxygen density, thus raising the G width of the oxidized spectra. Finally, the larger G for the oxidized clusters can be affected by fluctuation of the 1:1 Fe to O ratio: clusters possessing a slightly different stoichiometry cannot be resolved in the spectral analysis and hence contribute to the overall spectral broadening.

Our investigation suggests that the oxidation process of supported iron nanoclusters is quite different from the case of iron solid surfaces. At room temperature, the oxide growth on iron surfaces typically involves several layers, it proceeds mainly via inward oxygen diffusion across the interface between metal-oxide and gas and it leads to the formation of two oxide phases. The first phase consists of a layer of FeO that has the function of a wet layer for the subsequent growth of a second oxide phase composed of Fe_2O_3[81]. Indeed, FeO on a surface tends to oxidize rapidly to form compounds with Fe ions in the Fe(III) oxidation state[73,82]. On the contrary, we show that the oxidation process of Fe nanoclusters leads to a stable Fe(II) oxide compound, as confirmed by negligible Fe $2p_{3/2}$ spectral changes upon further oxygen exposure. It is important to stress out that the oxidation method that we employed providing atomic oxygen at very low temperatures is extremely efficient, as it was proved for the case of Pt(111)[67] and for the oxidation of size selected Ag clusters where atoms in the clusters reached an oxidation state 3+[43]. Conversely, the hindering towards a 3+ oxidation state in iron may be closely related to size of the unit cells of iron oxide compounds that include Fe(III) ions and higher density of oxygen atoms. For example, the unit cell of magnetite and maghemite accommodates 32 O^{2-} ions[16,83], while there are only 4 in the unit cell of wüstite (FeO)[16]. We expect formation of such a large unit cell to be strongly unfavorable just because lattice deformations are energetically very expensive.

Conclusions

In the present study, we investigated the oxidation of Fe_n nanoclusters with $n = 11$, 12, 13, 15 and 20 by means of high-resolution XPS. Metallic Fe clusters supported by Gr/Ru(0001) interface present a CLS towards higher binding energies with respect to iron bulk and solid surfaces. We attribute this phenomenon to lattice strain that generates a contraction of the Fe-Fe average interatomic distance of clusters with respect to bulk Fe. According to previous investigations, CLS are related also to the chemical reactivity of the system. In this respect we found that Fe clusters with larger CLS and lower asymmetry parameter are the most stable ones among the examined clusters. The BE of Fe clusters after the oxidation are more similar to bulk and surface oxide with respect to their metallic counterparts. The complete disappearance of the metallic component in Fe oxide clusters spectra paralleled by growth of a single new component at higher BE is interpreted as the formation of Fe clusters with a Fe to O ratio close to 1:1, in agreement with previous experiments of oxide clusters in gas phase. All Fe atoms in the clusters are in the Fe(II) oxidation state. Further oxygen exposures do not lead to any modification in Fe $2p_{3/2}$ core level spectra, suggesting that this is the most energetically favored configuration that clusters can reach upon photo-induced oxidation at a very low temperature. The difference between the oxidation of iron bulk and surfaces and iron nanoclusters is a clear proof that matter at the sub-nanoscale behaves in a different way. We believe that our results can help shedding light into the oxidation process at the nanoscale and into the use of supported Fe oxide nanoclusters in chemical reactions.

Methods

Sample preparation. The Ru(0001) crystal was cleaned through several cycles of sputtering and annealing. Sputtering cycles were made using Ar^+ ions ($E_{kin} = 3$ keV) while annealing cycles were made first in O_2 atmosphere to remove C by raising the temperature each cycle, from 600 K up to 1100 K and finally by a flash annealing to 1570 K to induce the oxygen desorption. Graphene was grown by thermal decomposition of ethylene (C_2H_4) in two steps. In the first one, Ru crystal was heated to 1100 K and exposed to ethylene for 300 s at a pressure of 2×10^{-8} mbar. In the second step, Ru crystal was kept at 1100 K and exposed to ethylene for 900 s at a pressure of 5×10^{-8} mbar. The quality of the grown graphene was checked by looking at the Low Energy Electron Diffraction image (Supplementary Fig. 3a), which shows the extra diffraction spots of the (13x13) moiré pattern, and at the C 1s core level spectrum (Supplementary Fig. 3b), which displays the typical double components due to weakly and highly interacting regions of the unit cell[84].

Fe clusters depostion and oxidation. Fe_{11}^+, Fe_{12}^+, Fe_{13}^+, Fe_{15}^+ and Fe_{20}^+ clusters were generated by using ENAC (Exact Number of Atoms in each Clusters), the size-selected clusters source based on the laser ablation process and quadrupole mass spectrometer (Extrel 150QC RF-DC, mass range m/z 10–16000 amu) mass selection[85,86] (Supplementary Fig. 4). Iron nanoclusters were deposited on graphene/Ru(0001) in a soft-landing regime, i.e. with a kinetic energy lower than 1 eV/atom to avoid clusters fragmentation[87]. The clusters coverage for each deposition was 0.06% ML, which ensures a statistical occupation of one iron cluster every 9 moiré cells, that is approximately one Fe cluster every 3000 carbon atoms. Depositions, chemical reactions, and measurements were performed at a temperature of 20 K to avoid clusters diffusion and nucleation.

High-resolution X-Ray photoelectron spectroscopy. High- Resolution X-Ray Photoelectron Spectroscopy measurements were performed at the SuperESCA beamline of the synchrotron light source Elettra, Trieste (IT). Photoemission spectra of the core level region Fe $2p_{3/2}$ were recorded for each cluster, tuning the photon energy to generate photoelectrons with a kinetic energy of about 100 eV to enhance surface sensitivity. The overall energy resolution at the employed photon energy ($h\nu = 805$ eV) was 200 meV. The intensity of each photoemission spectrum was normalized to the photon flux, while the binding energy (BE) scale was accurately calibrated by measuring the Fermi energy of the substrate. Each component of the photoemission spectra was fitted using a Doniach-Šunjić[46] function convoluted with a Gaussian distribution to account for experimental resolution, vibrational and inhomogeneous broadening. The analysis was performed using a polynomial background[88] which empirically resulted to be the most appropriate for our spectra.

Data availability

The data presented in this study are available from the corresponding author upon reasonable request.

Received: 11 November 2022; Accepted: 24 March 2023;
Published online: 03 April 2023

References

1. Jeong, H., Shin, S. & Lee, H. Heterogeneous atomic catalysts overcoming the limitation of single atom catalysts. *ACS Nano* **14**, 14355–14374 (2020).
2. Liu, L. & Corma, A. Metal catalysts for heterogeneous catalysis: from single atoms to nanoclusters and nanoparticles. *Chem. Rev.* **118**, 4981–5079 (2018).
3. Dong, C. et al. Supported metal clusters: fabrication and application in heterogeneous catalysis. *ACS Catal.* **10**, 11011–11045 (2010).
4. Tyo, E. C. & Vajda, S. Catalysis by clusters with precise numbers of atoms. *Nat. Nanotech.* **10**, 577–588 (2015).
5. Cui, C., Zhang, H. & Luo, Z. Nitrogen reduction reaction on small iron clusters supported by N-doped graphene: a theoretical study of the atomically precise active-site mechanism. *Nano Res.* **13**, 2280–2288 (2020).
6. Haber, F. & van Oordt, G. Über die bildung von ammoniak den elementen. *Z. f.ür. Anorganische Chem.* **44**, 341–378 (1905).
7. Ertl, G. Reactions at surfaces: From atoms to complexity (nobel lecture). *Angew. Chem. Int. Ed.* **47**, 3524–3535 (2008).

8. Cherkasov, N., Ibhadon, A. O. & Fitzpatrick, P. A review of the existing and alternative methods for greener nitrogen fixation. *Chem. Eng. Process.: Process Intensif.* **90**, 24–33 (2015).
9. Reuter, K., Plaisance, C. P., Oberhofer, H. & Andersen, M. Perspective: on the active site model in computational catalyst screening. *J. Chem. Phys.* **146**, 040901 (2017).
10. Zitolo, A. et al. Identification of catalytic sites for oxygen reduction in iron- and nitrogen-doped graphene materials. *Nat. Mater.* **14**, 937–942 (2015).
11. Ye, W. et al. Precisely tuning the number of Fe atoms in clusters on N-doped carbon toward acidic oxygen reduction reaction. *Chem* **5**, 2865–2878 (2019).
12. Yang, Z. et al. Subnano-FeO_x clusters anchored in an ultrathin amorphous Al_2O_3 nanosheet for styrene epoxidation. *ACS Catal.* **11**, 11542–11550 (2021).
13. Wan, X. et al. Iron atom-cluster interactions increase activity and improve durability in Fe − N − C fuel cells. *Nat. Commun.* **13**, 2963 (2022).
14. Liu, J. C. et al. Heterogeneous Fe_3 single-cluster catalyst for ammonia synthesis via an associative mechanism. *Nat. Commun.* **9**, 1610 (2018).
15. Tian, S. et al. Carbon nitride supported Fe_2 cluster catalysts with superior performance for alkene epoxidation. *Nat. Commun.* **9**, 2353 (2018).
16. Cornell, R. M. & Schwertmann, U. *The Iron Oxides: Structure, Properties, Reactions, Occurrences and Uses* (Wiley-VCH, 2003).
17. Laurent, S. et al. Magnetic iron oxide nanoparticles: synthesis, stabilization, vectorization, physicochemical characterizations, and biological applications. *Chem. Rev.* **108**, 2064–2110 (2008).
18. Sun, S., Murray, C. B., Weller, D., Folks, L. & Moser, A. Monodisperse fept nanoparticles and ferromagnetic FePt nanocrystal superlattices. *Science* **287**, 1989–1992 (2000).
19. Nikitin, A. A. et al. Synthesis of iron oxide nanoclusters by thermal decomposition. *Langmuir* **34**, 4640–4650 (2018).
20. Li, P., Miser, D. E., Rabiei, S., Yadav, R. T. & Hajaligol, M. R. The removal of carbon monoxide by iron oxide nanoparticles. *Appl. Catal. B* **43**, 151–162 (2003).
21. Šmit, G., Zrnčević, S. & Lázár, K. Adsorption and low-temperature oxidation of CO over iron oxides. *J. Mol. Catal. A: Chem.* **252**, 103–106 (2006).
22. Reilly, N., Reveles, J. U., Johnson, E. G., Khanna, S. N. & Castleman, A. W. Experimental and theoretical study of the structure and reactivity of $Fe_mO_n^+$ (m = 1, 2; n = 1–5) with CO. *J. Phys. Chem.* **111**, 19086–19097 (2007).
23. Xue, W., Wang, Z. C., He, S. G., Xie, Y. & Bernstein, E. R. Experimental and theoretical study of the reactions between small neutral iron oxide clusters and carbon monoxide. *J. Am. Chem. Soc.* **130**, 15879–15888 (2008).
24. Schlicher, S. et al. Quality or Quantity? How structural parameters affect catalytic activity of iron oxides for CO oxidation. *Catalysis* **12**, 675 (2022).
25. Steinfeld, A., Sanders, S. & Palumbo, R. Design aspects of solar thermochemical engineering—a case study: two step water-splitting cycle using the Fe_3O_4/FeO redox system. *Sol. Energy* **65**, 43–53 (1999).
26. Zhu, M. & Wachs, I. E. Iron-based catalysts for the High-Temperature Water-Gas Shift (HT-WGS) reaction: a review. *ACS Catal.* **6**, 722–732 (2015).
27. Reddy, B. V. & Khanna, S. N. Self-stimulated NO reduction and CO oxidation by iron oxide clusters. *Phys. Rev. Lett.* **93**, 068301 (2004).
28. Ju, M. et al. Systematic theoretical investigation of geometries, stabilities and magnetic properties of iron oxide clusters $(FeO)_n^\mu$ ($n = 1$–8, $\mu = 0, \pm 1$): insights and perspectives. *RCS Adv.* **5**, 6560–6570 (2015).
29. Gutsev, G. L., Belay, K. G., Gutsev, L. G., Ramachandran, B. R. & Jena, P. Effect of hydrogenation on the structure and magnetic properties of an iron oxide cluster. *Phys. Chem. Chem. Phys.* **20**, 4546–4553 (2018).
30. Yu, X., Oganov, A. R., Zhu, Q., Qi, F. & Qian, G. The stability and unexpected chemistry of oxide clusters. *Phys. Chem. Chem. Phys.* **20**, 30437–30444 (2018).
31. Yu, X., Oganov, A. R., Zhu, Q., Qi, F. & Qian, G. High coverage CO adsorption on Fe_6O_6 cluster using GGA + U. *J. Clust. Sci.* **31**, 591–600 (2020).
32. Aguilera-del Toro, R. H., Aguilera-Granja, F., Torres, M. B. & Vega, A. Relation between structural patterns and magnetism in small iron oxide clusters: reentrance of the magnetic moment at high oxidation ratios. *Phys. Chem. Chem. Phys.* **23**, 246–272 (2021).
33. Shin, D. N., Matsuda, Y. & Bernstein, E. R. On the iron oxide neutral cluster distribution in the gas phase. i. detection through 193 nm multiphoton ionization. *J. Chem. Phys.* **120**, 4150–4156 (2004).
34. Lv, S. L., Liu, Q. Y., Chen, J. J. & He, S. G. Oxidation of isoprene by neutral iron oxide nanoclusters in the gas phase. *J. Phys. Chem. C.* **123**, 25949–25956 (2019).
35. Chen, J. J., Yuan, Z., Li, X. N. & He, S. G. A VUV photoionization time-of-flight mass spectrometer for the formation, distribution, and reaction of nano-sized neutral metal oxide clusters. *Int. J. Mass Spectrom.* **422**, 98–104 (2017).
36. Garcia, J. M., Shaffer, R. E. & Sayres, S. G. Ultrafast pump-probe spectroscopy of neutral Fe_nO_m clusters (n, m < 16). *Phys. Chem. Chem. Phys.* **22**, 24624–24632 (2020).
37. Aktüka, A. & Sebetci, A. BH-DFTB/DFT calculations for iron clusters. *AIP Adv.* **6**, 055103 (2016).
38. Sakurai, M., Watanabe, K., Sumiyama, K. & Suzuki, K. Magic numbers in transition metal (Fe, Ti, Zr, Nb, and Ta) clusters observed by time-of-flight mass spectrometry. *J. Chem. Phys.* **111**, 235–238 (1999).
39. Wang, L. J. Photoelectron spectroscopy of size selected transition metal clusters: Fe_n^-, $n = 3$-24. *J. Chem. Phys.* **102**, 9480–9493 (1995).
40. Yu, X., Zhang, X. & Yan, X. Stability of the $Fe_{12}O_{12}$ cluster. *Nano Res.* **11**, 3574–3581 (2018).
41. Gutsev, G. L., Belay, K. G., Gutsev, L. G. & Ramachandrand, B. R. Geometrical and magnetic structure of iron oxide clusters $(FeO)_n$ for $n > 10$. *Comp. Mat. Sci.* **137**, 134–143 (2017).
42. Zhang, H., Fu, Q., Cui, Y., Tan, D. & Bao, X. Growth mechanism of graphene on Ru(0001) and O_2 adsorption on the graphene/Ru(0001) surface. *J. Phys. Chem. C.* **113**, 8296–8301 (2009).
43. Loi, F. et al. Oxidation at the sub-nanoscale: oxygen adsorption on graphene-supported size-selected Ag clusters. *J. Mater. Chem. A* **10**, 14594–14603 (2022).
44. Habenicht, B. F., Teng, D., Semidey-Flecha, L., Sholl, D. S. & Xu, Y. Adsorption and diffusion of 4d and 5d transition metal adatoms on graphene/Ru(0001) and the implications for cluster nucleation. *Top. Catal.* **57**, 69–79 (2014).
45. Liu, X. et al. Metals on graphene: correlation between adatom adsorption behaviour and growth morphology. *Phys. Chem. Chem. Phys.* **14**, 9157–9166 (2012).
46. Doniach, S. & Sunjic, M. Many-electron singularity in x-ray photoemission and x-ray line spectra from metals. *J. Phys. C: Solid State Phys.* **3**, 285–291 (1970).
47. Herrera-Gomez, A. et al. A self-consistent multiple-peak structure of the photoemission spectra of metallic Fe 2p as a function of film thickness. *Surf. Interface Anal.* **52**, 591–599 (2020).
48. Blomberg, S. et al. The structure of the $Rh_2O_3(0001)$ surface. *Surf. Sci.* **606**, 1416–1421 (2012).
49. Zemlyanov, D. et al. Kinetics of Palladium oxidation in the mbar pressure range: ambient pressure XPS study. *Top. Catal.* **56**, 885–895 (2013).
50. Blomberg, S. et al. A high pressure X-ray photoelectron spectroscopy study of oxidation and reduction of Rh(100) and Rh nanoparticles. *Surf. Sci.* **628**, 153–158 (2014).
51. Mikkelä, M. H. et al. Size-dependent study of Rb and K clusters using core and valence level photoelectron spectroscopy. *Eur. Phys. J. D.* **64**, 347–352 (2011).
52. Bano, A., Patra, L. & Pandey, R. Stability and electronic properties of the graphene-supported FeO nanostructures including clusters and monolayer. *Appl. Surf. Sci.* **569**, 150976 (2021).
53. Hillebrecht, F. U., Roth, C., Rose, H. B., Park, W. G. & Kisker, E. Magnetic linear dichroism in spin-resolved Fe 2p photoemission. *Phys. Rev. B* **53**, 12182–12195 (1996).
54. Rossi, G. et al. Magnetic dichroism in the angular distribution of Fe 2p and 3p photoelectrons: empirical support to Zeeman-like analysis. *Phys. Rev. B* **55**, 11488–11495 (1997).
55. Weissenrieder, J. et al. Oxygen structures on Fe(110). *Surf. Sci.* **527**, 163–172 (2003).
56. Biesinger, M. C. et al. Resolving surface chemical states in XPS analysis of first row transition metals, oxides and hydroxides: Cr, Mn, Fe, Co and Ni. *Appl. Surf. Sci.* **257**, 2717–2730 (2011).
57. de Mendonça, R., Martins, M. D., Silly, M., Sirotti, F. & Macedo, W. A. A. A photoemission spectroscopy study of the initial oxidation of epitaxial fcc and bcc Fe films grown on Cu(100). *Thin Solid Films* **636**, 567–572 (2017).
58. Kaden, W. E., Wu, T., Kunkel, W. A. & Anderson, S. L. Electronic structure controls reactivity of size-selected Pd clusters adsorbed on TiO_2 surfaces. *Science* **102**, 826–829 (2009).
59. Peters, S., Peredkov, S., Neeb, M., Eberhardt, W. & Al-Hada, M. Size-dependent XPS spectra of small supported Au-clusters. *Surf. Sci.* **608**, 129–134 (2013).
60. Henry, C. R., Chapon, C., Goyhenex, C. & Monot, R. Size effect in the CO chemisorption on palladium clusters supported on magnesium oxide. *Surf. Sci.* **272**, 283–288 (1992).
61. Richter, B., Kuhlenbeck, H., Freund, H. J. & Bagus, P. S. Cluster core-level binding-energy shifts: The role of lattice strain. *Phys. Rev. Lett.* **93**, 026805 (2004).
62. Bagus, P. S., Wieckowski, A. & Freund, H. The contribution of lattice strain to core-level binding energy shifts in metal nanoparticles: Generality and origin of the shifts. *Comput. Theor. Chem.* **987**, 22–24 (2012).
63. Davey, W. P. Precision measurements of the lattice constants of twelve common metals. *Phys. Rev.* **25**, 753–761 (1995).
64. Kuivila, C. S., Butt, J. B. & Stair, P. C. Characterization of surface species on iron synthesis catalysts by x-ray photoelectron spectroscopy. *Appl. Surf. Sci.* **32**, 99–121 (1988).
65. Hammer, B. & Norskov, J. K. Theoretical surface science and catalysis—calculations and concepts. *Adv. Catal.* **45**, 71–129 (2000).
66. Van Santen, R. A. & Neurock, M. Concepts in theoretical heterogeneous catalytic reactivity. *Catal. Rev. Sci. Eng.* **37**, 557–698 (1995).
67. Kim, Y. S. et al. The study of oxygen molecules on Pt(111) surface with high resolution x-ray photoemission spectroscopy. *J. Chem. Phys.* **133**, 034501 (2010).

68. Sprodowski, C., Mehlhorn, M. & Morgenstern, K. Dissociation of oxygen on Ag(100) induced by inelastic electron tunneling. *J. Phys. Condens. Matter* **22**, 264005 (2010).
69. Jiang, P. et al. Room-temperature reaction of oxygen with gold: an in situ ambient-pressure x-ray photoelectron spectroscopy investigation. *J. Am. Chem. Soc.* **132**, 2858–2859 (2010).
70. Cosby, P. C. Electron-impact dissociation of nitrogen. *J. Chem. Phys.* **98**, 9544–9553 (1993).
71. Stipe, B. C., Rezaei, M. A. & Ho, W. Atomistic studies of O_2 dissociation on Pt(111) induced by photons, electrons, and by heating. *J. Chem. Phys.* **107**, 6443–6447 (1997).
72. Stipe, B. C. et al. Single-molecule dissociation by tunneling electrons. *Phys. Rev. Lett.* **78**, 4410–4113 (1997).
73. Roosendaal, S. J., van Asselen, B., Elsenaar, J. W., Vredenberg, A. M. & Habraken, F. H. P. M. The oxidation state of Fe(100) after initial oxidation in O_2. *Surf. Sci.* **442**, 329–337 (1999).
74. Davies, R. et al. The oxidation of Fe(111). *Surf. Sci.* **605**, 1754–1762 (2011).
75. Lin, T. C., Seshadri, G. & Kelber, J. A. A consistent method for quantitative XPS peak analysis of thin oxide films on clean polycrystalline iron surfaces. *Appl. Surf. Sci.* **119**, 83–92 (1997).
76. Grosvenor, A. P., Kobe, B. A., Biesinger, M. C. & McIntyre, N. S. Investigation of multiplet splitting of Fe 2p XPS spectra and bonding in iron compounds. *Surf. Interface Anal.* **36**, 1564–1574 (2004).
77. Sun, Q. et al. First-principles studies on the intrinsic stability of the magic Fe_{13O8} cluster. *Phys. Rev. B* **61**, 5781–5785 (2000).
78. Nelin, C. J. et al. Surface core-level binding energy shifts for MgO(100). *Phys. Chem. Chem. Phys.* **16**, 21953–21956 (2004).
79. Bagus, P. S. et al. Revisiting surface core-level shifts for ionic compounds. *Phys. Rev. B* **100**, 115419 (2019).
80. Jones, N. O., Reddy, B. V., Rasouli, F. & Khanna, S. N. Erratum: Structural growth in iron oxide clusters: Rings, towers, and hollow drums. *Phys. Rev. B* **73**, 119901 (2006).
81. Subbaraman, R., Deshmukh, S. A. & Sankaranarayanan, S. K. R. S. Atomistic insights into early stage oxidation and nanoscale oxide growth on Fe(100), Fe(111) and Fe(110) surfaces. *J. Phys. Chem. C.* **117**, 5195–5207 (2013).
82. Bagus, P. S. et al. Combined multiplet theory and experiment for the fe 2p and 3p XPS of FeO and Fe_2O_3. *J. Chem. Phys.* **154**, 094709 (2021).
83. Parkinson, G. S. Iron oxide surfaces. *Surf. Sci. Rep.* **71**, 272–365 (2016).
84. Alfè, D. et al. Fine tuning of graphene-metal adhesion by surface alloying. *Sci. Rep.* **3**, 2430 (2013).
85. Sbuelz, L. et al. Atomic undercoordination in Ag islands on Ru(0001) grown via size-selected cluster deposition: an experimental and theoretical high-resolution core-level photoemission study. *J. Phys. Chem. C.* **125**, 9556–9563 (2021).
86. Loi, F. et al. Breakdown of the correlation between oxidation states and core electron binding energies at the sub-nanoscale. *Appl. Surf. Sci.* **619**, 156755 (2023).
87. Binnis, C. Nanoclusters deposited on surfaces. *Surf. Sci. Rep.* **44**, 1–49 (2001).
88. Sickafus, E. N. Linearized secondary-electron cascades from the surfaces of metals. I. Clean surfaces of homogeneous specimens. *Phys. Rev. B* **16**, 1436–1447 (1977).

Acknowledgements

The authors thank Elettra-Sincrotrone Trieste for the support received during the beamtime allocated at the SuperESCA beamline. We thank G. Panaccione and J. Fuji for very fruitful discussions. A.B. acknowledges funding from the University of Trieste through the METAMAT project. L.B. acknowledges funding from the University of Trieste through the D55 Microgrants funding initiative. U.H and A.K. acknowledge funding from DFG (HE3454/23-2).

Author contributions

A.B. conceived the project and coordinated the research activities. A.K., U.H. and A.B. designed the cluster source. D.P., F.L., L.S. and L.B. performed the set-up of the cluster source and did the cluster deposition. P.L. and S.L. performed the set-up of the Super-ESCA beamline. D.P., F.L., L.B., L.S, P.L., E.T, S.L. and A.B. acquired the X-ray Photo-electron Spectroscopy data. D.P. carried out the experimental data analysis. D.P., F.L and A.B. wrote the manuscript. All authors extensively discussed the results and the inter-pretation and revised the manuscript.

Competing interests

The authors declare no competing interests.

Additional information

Supplementary information The online version contains supplementary material available at https://doi.org/10.1038/s42004-023-00865-x.

Correspondence and requests for materials should be addressed to Alessandro Baraldi.

Peer review information *Communications Chemistry* thanks the anonymous reviewers for their contribution to the peer review of this work.

Reprints and permission information is available at http://www.nature.com/reprints

Publisher's note Springer Nature remains neutral with regard to jurisdictional claims in published maps and institutional affiliations.

Open Access This article is licensed under a Creative Commons Attribution 4.0 International License, which permits use, sharing, adaptation, distribution and reproduction in any medium or format, as long as you give appropriate credit to the original author(s) and the source, provide a link to the Creative Commons license, and indicate if changes were made. The images or other third party material in this article are included in the article's Creative Commons license, unless indicated otherwise in a credit line to the material. If material is not included in the article's Creative Commons license and your intended use is not permitted by statutory regulation or exceeds the permitted use, you will need to obtain permission directly from the copyright holder. To view a copy of this license, visit http://creativecommons.org/licenses/by/4.0/.

© The Author(s) 2023